

Chapter 6

Numerical examples for linear analysis.

This Chapter presents numerical examples of several linear test problems. These are used to validate the formulation of the linear ANDES elements that represents the “kernel” of the co-rotational formulation.

6.1 Patch tests.

The Patch Test has become a standard test for evaluation of new finite elements. Though neither a necessary or sufficient condition for convergence, it has a strong following who considers the test “necessary” for an element to be considered reliable. However, there is little disagreement about the tests value as a debugging tool when an element is implemented in an actual finite element code.

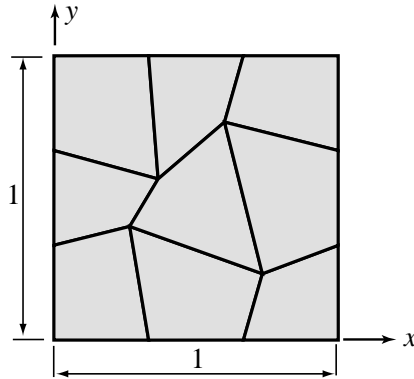


Figure 6.1. Patch test for quadrilateral elements.

The patch shown on Figure 6.1 has been used to perform the patch test for the new ANDES4 element by giving the boundary nodes displacements according to a constant strain pattern. The patch test requires that the internal nodes get displacements that satisfies this constant strain displacement mode exactly.

Membrane tests.

$$u = x \quad \Rightarrow \quad \epsilon_{xx} = \frac{\partial u}{\partial x} = 1 \quad : \quad \text{Identically satisfied.}$$

$$v = y \quad \Rightarrow \quad \epsilon_{yy} = \frac{\partial v}{\partial y} = 1 \quad : \quad \text{Identically satisfied.}$$

$$u = y, v = x \quad \Rightarrow \quad \gamma_{xy} = \left(\frac{\partial u}{\partial y} + \frac{\partial v}{\partial x} \right) = 2 \quad : \quad \text{Identically satisfied.}$$

Bending tests.

$$w = x^2 \quad \Rightarrow \quad \kappa_{xx} = \frac{\partial^2 w}{\partial x^2} = 2 \quad : \quad \text{Identically satisfied.}$$

$$w = y^2 \quad \Rightarrow \quad \kappa_{yy} = \frac{\partial^2 w}{\partial y^2} = 2 \quad : \quad \text{Identically satisfied.}$$

$$w = xy \quad \Rightarrow \quad \kappa_{xy} = 2 \frac{\partial^2 w}{\partial x \partial y} = 2 \quad : \quad \text{Identically satisfied.}$$

The membrane patch test for the ANDES4 element are satisfied regardless of whether the higher order strain displacement matrix \mathbf{B}_h or the deviatoric higher order strain displacement matrix $\mathbf{B}_d = \mathbf{B}_h - \bar{\mathbf{B}}_h$ is used for the higher order membrane stiffness according to equation (0.0.0) and (0.0.0).

6.2 Membrane problems.

6.2.1 Shear-loaded cantilever beam.

A shear loaded cantilever beam is defined according to Figure 8.1. This Figure also shows the 16×4 regular and irregular element meshes.

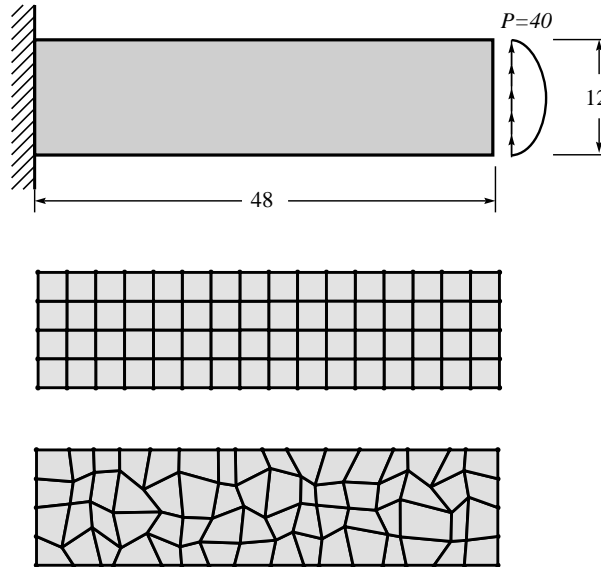


Figure 6.2. Cantilever under end shear. $E = 30000$ $\nu = 0.25$

The test has been run using a totally clamped boundary at the fixed end, and the applied nodal forces on the end cross-section are consistent lumping of a shear load with parabolic variation in the y -direction.

The comparison value is the tip deflection of 0.35583 at the end of the beam. This number is the exact solution of the two-dimensional plane stress as given in [28]. The numerical results have been scaled so that the analytical displacement of 0.35583 corresponds to 100 in Table 6.1. Table 6.1 also includes numerical results for the quadrilateral FFQ and the triangular FFT as described by Nygård in [47].

Table 6.1. Tip deflection of cantilever beam.

Element	$x \times y$ -subdivisions				
	4×1	8×2	16×4	32×8	64×16
Regular element mesh					
CST	25.48	55.24	82.66	94.96	98.71
QSHELL3	111.78	101.18	100.03	99.97	100.01
QSHELL4	97.72	98.86	99.54	99.87	100.00
Irregular element mesh					
CST	27.86	55.84	81.47	94.27	98.41
QSHELL3	98.16	100.12	99.66	99.87	99.97
QSHELL4	103.93	98.60	99.45	99.90	100.01

Table 6.1 shows very similar convergence rates for the QSHELL3 and QSHELL4 element compared to Nygård's FFT and FFQ element. However, the ANDES elements tend to be more flexible for very coarse meshes.

6.3 Bending problems.

6.3.1 Centrally loaded square plate.

A square plate subjected to a central load of $P = 40.0$. The test has been run with both simply supported and fully clamped boundary conditions.

Plate dimensions are 100.0×100.0 with thickness $t = 2.0$ and material properties $E = 1500.0$ and $\nu = 0.2$. Due to symmetry only a quarter of the plate have been modeled.

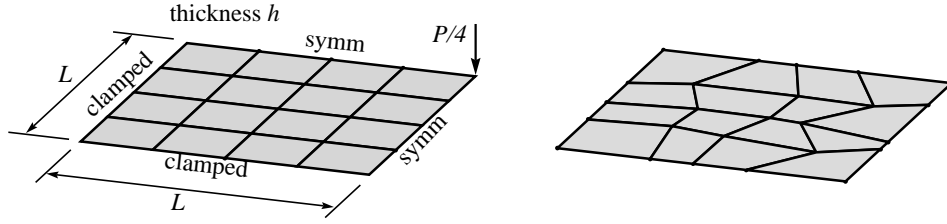


Figure 6.3. 4×4 quarter model of centrally loaded square plate.

Table 6.2. Central deflection of square plate with clamped boundary. Displacement 2.1552 is scaled to 100.00 .

Element type	Mesh over quarter plate					
	1×1	2×2	4×4	8×8	16×16	32×32
Regular mesh.						
BCIZ-SQ	88.223	102.71	101.18	100.37	100.10	100.02
ANDES3	92.798	103.75	101.57	100.50	100.15	100.04
ANDES4	88.944	100.07	100.18	100.07	100.02	100.00
Irregular mesh.						
BCIZ-SQ	88.223	99.805	101.27	99.781	99.983	99.938
ANDES3	92.798	102.48	102.38	100.40	100.23	100.02
ANDES4	88.944	99.793	101.71	100.19	100.14	100.02

6.4 Shell problems.

6.4.1 Pinched cylinder problem.

An open cylinder is subjected to two diametrically opposite point loads. Due to symmetry only 1/8 of the problem is modeled. The geometry of the 1/8 model is shown in Figure 6.4.

The mesh has been given an increasing distortion angle θ . As θ increases the four node elements are no longer flat elements. This induced warping gives different results for the projected and unprojected versions of the ANDES4 element. The ANDES3 element is invariant under projection because the element always possesses the correct rigid body modes.

The improvement with the projected stiffness matrix for the ANDES4 element is dramatic. This example displays the importance of correct rigid body modes, as well as showing the robustness of the stiffness projection procedure.

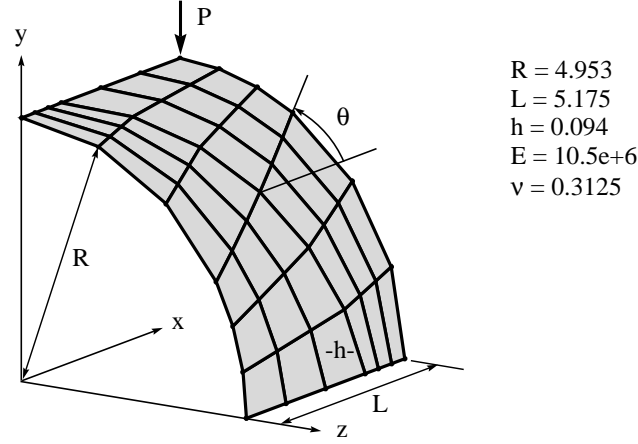


Figure 6.4. Pinched cylinder problem.

Table 6.3. Vertical displacement under load for pinched cylinder. Displacement 4.5301×10^{-3} is scaled to 100.00.

Element type	Distortion angle				
	$\theta = 0^\circ$	$\theta = 10^\circ$	$\theta = 20^\circ$	$\theta = 30^\circ$	$\theta = 40^\circ$
ANDES3 Unproj	99.578	99.136	98.737	98.296	97.608
ANDES3 Proj	99.578	99.136	98.737	98.296	97.608
ANDES4 Unproj	99.430	30.594	12.652	9.381	7.960
ANDES4 Proj	99.430	99.334	99.255	99.125	98.789

6.4.2 Pinched hemisphere problem.

A hemispherical shell is subjected to two pairs of diametrically opposite loads along the x and y axis respectively. Due to symmetry only a 1/4 model is used according to Figure 6.5.

This problem is often modelled with a hole at the top of the hemisphere. This allows using a mesh of strictly flat quadrilateral elements, which makes the test much less demanding for quadrilateral elements. One has chosen to model the hemisphere without a hole since this gives warped elements for the quadrilateral element meshes, and thus poses a much more severe test for those elements.

For the triangular ANDES3 two discretizations are used. Mesh 1 in Table 6.4 refers to a mesh where two triangular elements join at the loaded nodes, whereas Mesh 2 has one element attached to the loaded nodes.

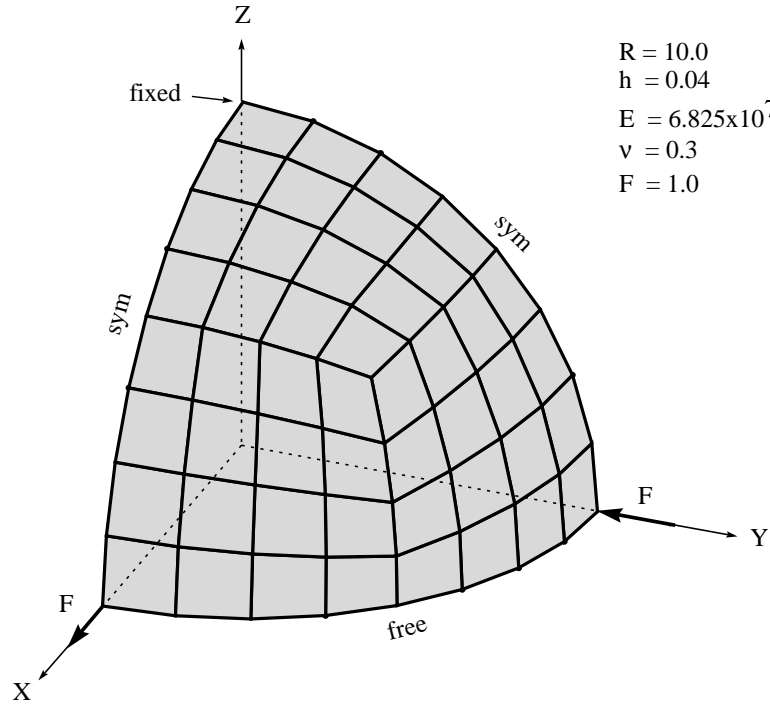


Figure 6.5. Pinched hemisphere problem.

Table 6.4. Displacements under loads for pinched hemisphere. Displacement 9.1898×10^{-2} is scaled to 100.00.

Element type	Elements per side					
	2	4	8	12	16	20
ANDES3 Mesh 1	0.18	2.59	25.30	61.44	83.23	92.52
ANDES3 Mesh 2	0.42	4.07	31.91	68.23	86.85	94.23
ANDES4 Unproj	13.57	6.13	12.85	19.49	25.17	30.18
ANDES4 Proj	67.55	23.73	85.53	97.24	99.39	100.00

This test again shows the dramatic improvement of the performance of the ANDES4 element when the stiffness projection is used.

Chapter 7

Numerical examples for linearized buckling analysis.

7.1 Buckling analysis of square plate compressed in one direction.

The buckling of a square plate subjected to in-plane uniaxial compression is considered. The geometry and material constants of the plate are given in Figure 7.1. The plate is simply supported along all edges with the in-plane deformations being unconstrained.

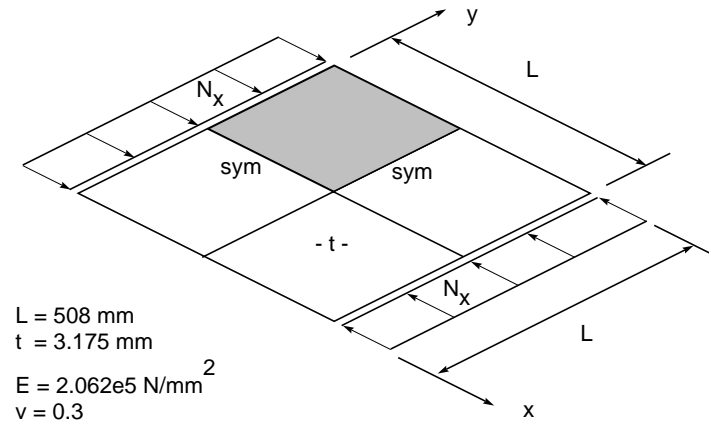


Figure 7.1. Square plate subjected to uniaxial compression.

The plate is compressed in its middle plane by a uniform load N_x along the edges $x = 0$ and $x = L$. Timoshenko [63] gives the analytical critical value of the compressive force per unit length as

$$(N_x)_{cr} = \frac{\pi^2 D}{L^2} \left(m + \frac{1}{m}\right)^2 \quad \text{where} \quad D = \frac{Et^3}{12(1 - \nu^2)}. \quad (7.1.1)$$

where L is plate side length, t is the plate thickness, ν is the Poisson's ratio and m is the number of half-waves in the compressive direction. The buckling modes are associated with odd values of m .

The geometric stiffness is based on the incremental solution at a load level of 1% of the critical load level. The results from the numerical analysis is tabulated in Table 7.2 and compared to results obtained by Bj  rum [17] with

the QSEL and FFQC elements. The QSEL and FFQC elements performs better than ANDES3 and ANDES4 for the higher order buckling modes. This is due to the “tuned” higher order geometric stiffness matrix used for those elements. However the geometric stiffness matrices used for the QSEL and FFQC element do not give a consistent tangent stiffness for nonlinear continuation analysis.

Table 7.1. Numerical results of square plate subjected to compression, normalized by the analytical solution of the first mode ($m = 1$).

Element Type	Analytical Solution	Mesh used for quarter of plate			
		4×4	8×8	16×16	32×32
ANDES3	$m = 1$: 1.000	1.008	1.002	1.000	1.000
	$m = 3$: 2.778	3.070	2.854	2.797	2.783
	$m = 5$: 6.760	8.342	7.270	6.893	6.798
ANDES4	$m = 1$: 1.000	1.043	1.011	1.002	1.001
	$m = 3$: 2.778	3.278	2.898	2.808	2.786
	$m = 5$: 6.760	10.11	7.522	6.950	6.815
QSEL	$m = 1$: 1.000	1.010	1.002	1.001	1.000
	$m = 3$: 2.778	3.032	2.840	2.793	2.782
	$m = 5$: 6.760	8.751	7.265	6.884	6.791
FFQC	$m = 1$: 1.000	0.973	0.993	0.998	1.000
	$m = 3$: 2.778	2.673	2.745	2.769	2.778
	$m = 5$: 6.760	6.750	6.694	6.738	6.754

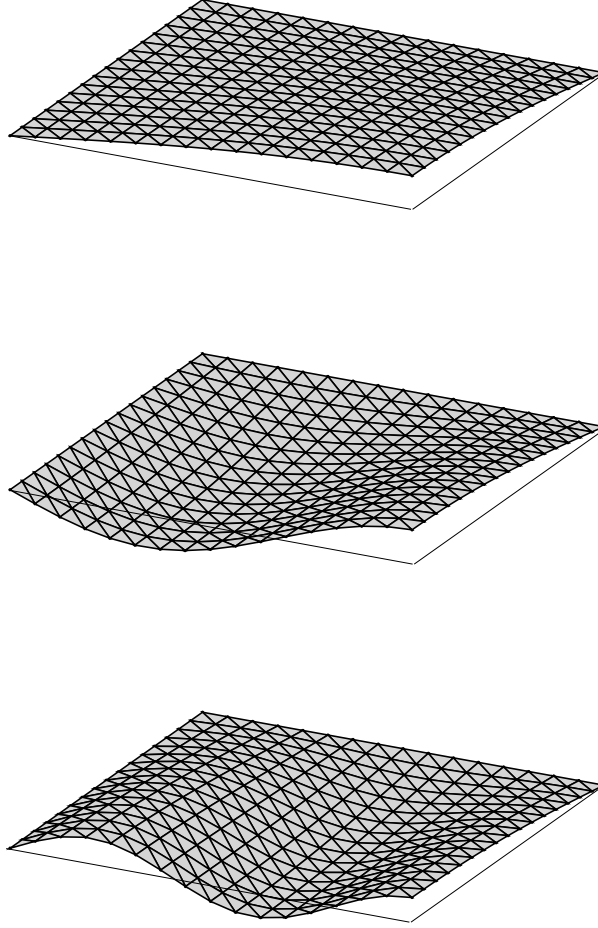


Figure 7.2. Buckling modes for $m = 1, 3$ and 5 according to equation (7.1.1) for square plate subjected to uniaxial compression.

7.2 Buckling analysis of shear loaded square plate.

A simply supported square plate with geometry and material constants given in Figure 7.3 is subjected to shear loads uniformly applied along the edges. The out-of-plane displacements and rotations are constrained whereas the in-plane rotations and translations along the boundaries are left free.

The critical shear force associated with the first buckling mode is give analytically by Timoshenko [63] as

$$(N_{xy})_{cr} = 9.34 \frac{\pi^2 D}{L^2} \quad \text{where} \quad D = \frac{Et^3}{12(1 - \nu^2)}. \quad (7.2.1)$$

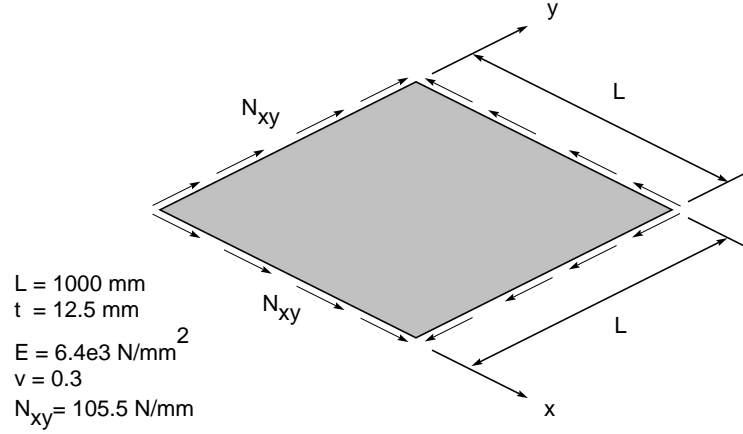


Figure 7.3. Square plate subjected to shear load.

Table 7.2. Numerical results of square plate subjected to shear, normalized by the analytical solution $(N_{xy})_{cr} = 105.5 \frac{N}{mm}$.

Element Type		Mesh used for the plate				
		4×4	8×8	16×16	32×32	64×64
ANDES3	$m = 1$:	1.446	1.145	1.057	1.013	
	$m = 2$:	2.174	1.293	1.240	1.238	
	$m = 3$:	8.631	2.974	2.709	2.675	
ANDES4	$m = 1$:	2.175	1.297	1.088	1.022	
	$m = 2$:	3.079	1.528	1.298	1.250	
	$m = 3$:		4.300	3.013	2.739	
QSEL	$m = 1$:	1.387	1.065	1.008	0.997	0.993
	$m = 2$:	2.096	1.385	1.268	1.242	1.233
	$m = 3$:	207.3	3.582	2.840	2.691	2.642
FFQC	$m = 1$:	0.781	0.908	0.967	0.987	0.994
	$m = 2$:	1.060	1.144	1.206	1.227	1.233
	$m = 3$:	2.073	2.301	2.518	2.614	2.643

This problem again shows that the higher order geometric stiffness matrix for the QSEL and FFQC element outperforms the consistent geometric stiffness matrix of the ANDES elements for linearized buckling analysis. The ANDES3 element performs better than the ANDES4 element simply because

meshes of $N \times N$ elements contains twice as many ANDES3 elements as ANDES4 elements since two triangles are required to fill one quadrilateral. This gives a “finer” discretization with respect to the rigid body displacements and thus a better global geometric stiffness matrix.

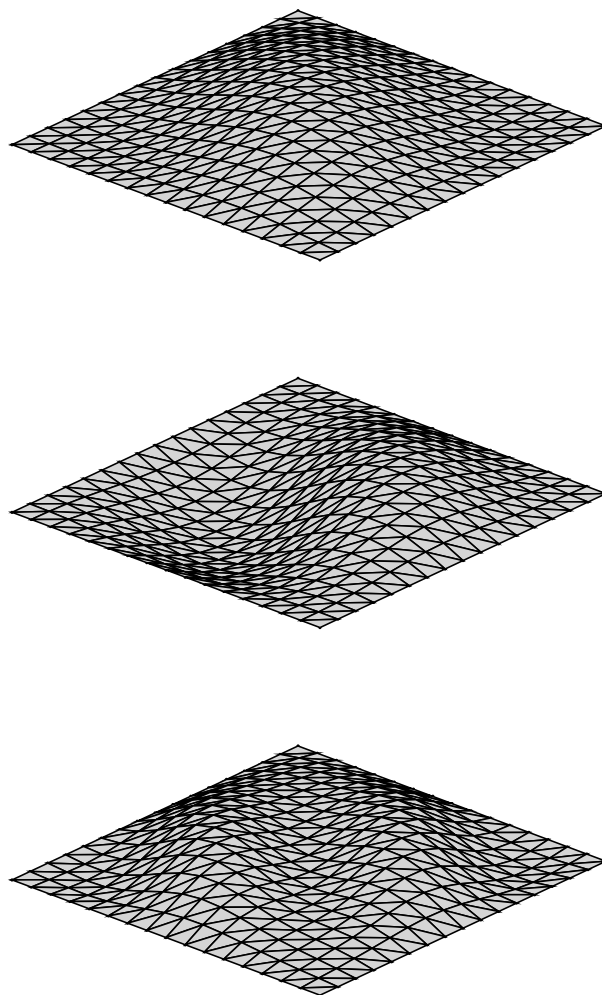


Figure 7.4. First three buckling modes for shear loaded square plate.

Chapter 8

Numerical examples for nonlinear analysis.

8.1 Smooth path following problems.

8.1.1 Cantilever beam subjected to end moment.

The cantilever in Figure 6.2 is used to demonstrate the large rotation and large displacement capabilities. The problem is usually formulated so that bending about one of the global axes takes place. The cantilever here is oriented arbitrarily in space so that the example becomes more demanding as regards the treatment of finite rotations as non-vectorial quantities. The position of the cantilever is defined by the auxiliary coordinate system

$$\begin{Bmatrix} \bar{x} \\ \bar{y} \\ \bar{z} \end{Bmatrix} = \frac{1}{7} \begin{bmatrix} 6 & -2 & -3 \\ 3 & 6 & 2 \\ 2 & -3 & 6 \end{bmatrix} \begin{Bmatrix} x \\ y \\ z \end{Bmatrix}, \quad (8.1.1)$$

and letting one side of the cantilever follow the \bar{x} -axis. This auxiliary system is used for modeling purposes only. The actual computations take place in the global (x, y, z) -system.

The exact solution is obtained from Bernoulli-Euler beam theory, and gives the deflected shape of the beam as a circle with radius

$$R = \frac{EI}{M_{\bar{y}}}. \quad (8.1.2)$$

This gives the tip deflections as

$$\frac{\bar{w}}{L} = \frac{EI}{M_{\bar{y}}L} \left(1 - \cos \frac{M - \bar{y}L}{EI}\right) \quad \text{and} \quad \frac{\bar{v}}{L} = -\frac{EI}{M_{\bar{y}}L} \sin \frac{M - \bar{y}L}{EI} \quad (8.1.3)$$

where \bar{w} and \bar{v} are the deflections in the \bar{x} - and \bar{z} - directions.

The problem was solved using load control with the incremental load steps $\Delta M_{\bar{y}} = \frac{2\pi}{40} \frac{ML}{EI}$, thus requiring 40 steps to bend the beam into a full circle. This small load step was required for the triangular element due to the large unbalanced membrane forces that are introduced during the iterations. The triangular element does not give symmetry about the center line of the cantilever, and thus converges more slowly than a comparable four node element,

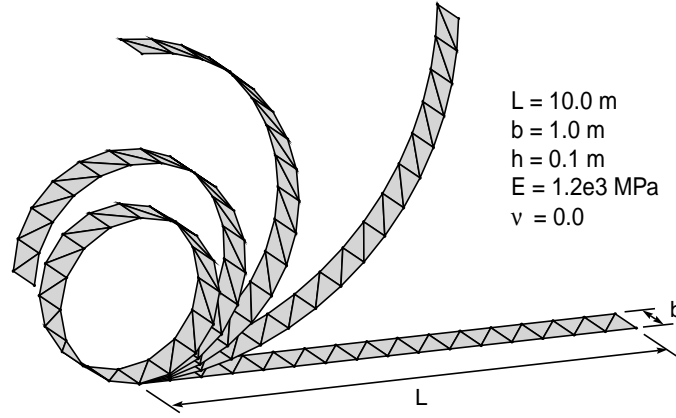


Figure 8.1. Cantilever oriented arbitrarily in space subjected to end moment.

as described by Nygård [47]. For the ANDES4 element the beam was bent into a full circle using 10 load steps.

Table 8.1 gives convergence rates and number of iterations for the cantilever modeled with 20 ANDES3 elements. The label “Fit type” refers to the \mathbf{G} matrix used for fitting the shadow element, with 1, 2 and 3 signifying side 12 alignment, least square fit of side edge angular errors and CST rotation, respectively. “1 diag” means that side 12 is directed along the diagonal of a rectangle assembly of two elements whereas “1 edge” means that side 12 is directed along the beam axis. Table 8.1 illustrates two points: Side 12 alignment is not orientation invariant since it doubles the number of iterations of the “1 diag” mesh compared to “1 edge”. Also, the applied load is a moment load, which gives a geometric stiffness that does not go towards symmetry as equilibrium is approached. The symmetrized stiffness will thus give poor convergence compared to the nonsymmetric tangent stiffness.

Table 8.1. Iterations for the first 10 steps.

Symmetric stiffness											
Fit type	Num. of iterations										Conv.
1 edge.	4	4	5	5	6	7	8	8	8	9	L
1 diag.	9	9	9	9	9	10	11	9	10	10	L
2	5	5	5	6	6	7	8	8	8	8	L
3	4	4	5	5	6	7	8	8	8	9	L
Non-symmetric stiffness											
Fit type	Num. of iterations										Conv.
1 edge.	4	4	4	4	4	4	4	4	4	4	Q
1 diag.	8	8	8	9	8	8	9	9	9	9	Q
2	5	5	5	5	5	5	5	5	5	5	Q
3	4	4	4	4	4	4	4	4	4	4	Q

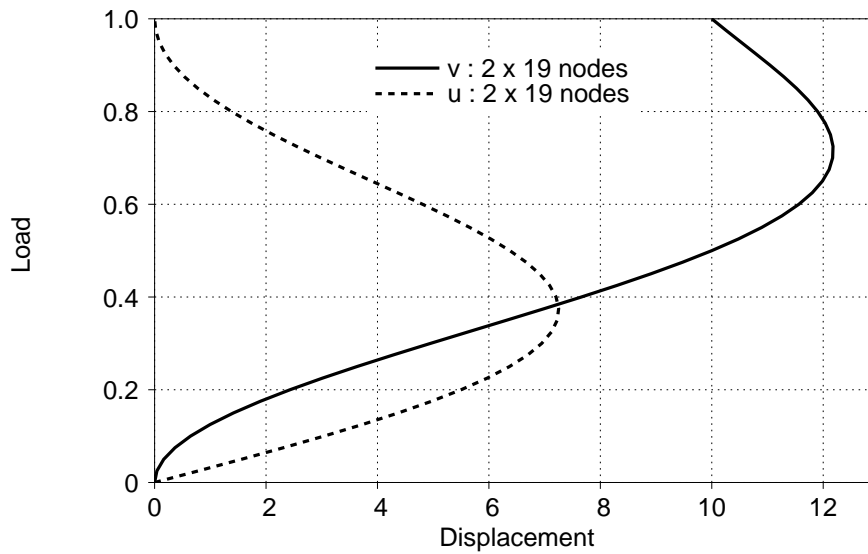


Figure 8.2. Tip displacements of the cantilever beam subjected to end moment.

8.1.2 Hinged cylindrical shell under concentrated load.

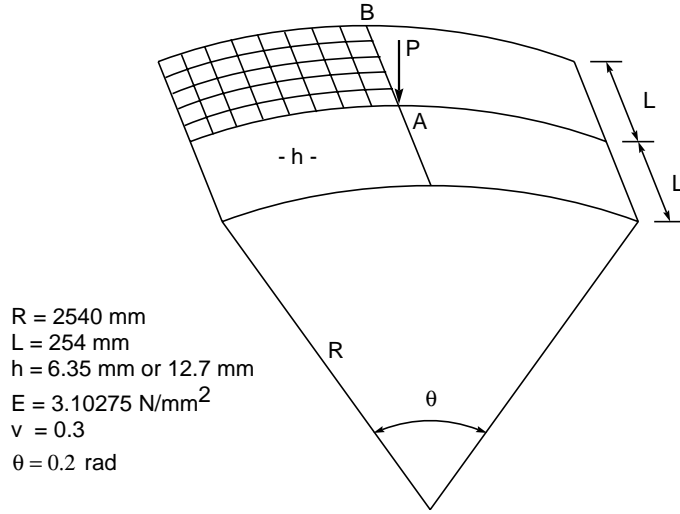


Figure 8.3. Geometry and material properties for hinged cylindrical shell.

The hinged cylindrical shell subjected to concentrated load is a common test case for geometrical nonlinearities. Nygård [47] performs an extensive comparison with other elements. Bjærum [17] gives a thorough comparison of different path-following algorithms for this example. The thinner shell of thickness $h = 6.35 \text{ mm}$ has a dramatic snap-back behavior well suited for verifying path following capabilities of the solution algorithm.

One quarter of the shell has been modeled using 8×8 rectangular units of two three node elements. The actual equilibrium path shown in Figures 8.4 and 8.5 agrees well with results obtained by Nygård [47].

The arc-length algorithm did not evidence convergence difficulties. With the thin shell the path has been followed using 26 steps and convergence was obtained within 5 iterations even at the snap-back section of the equilibrium path.

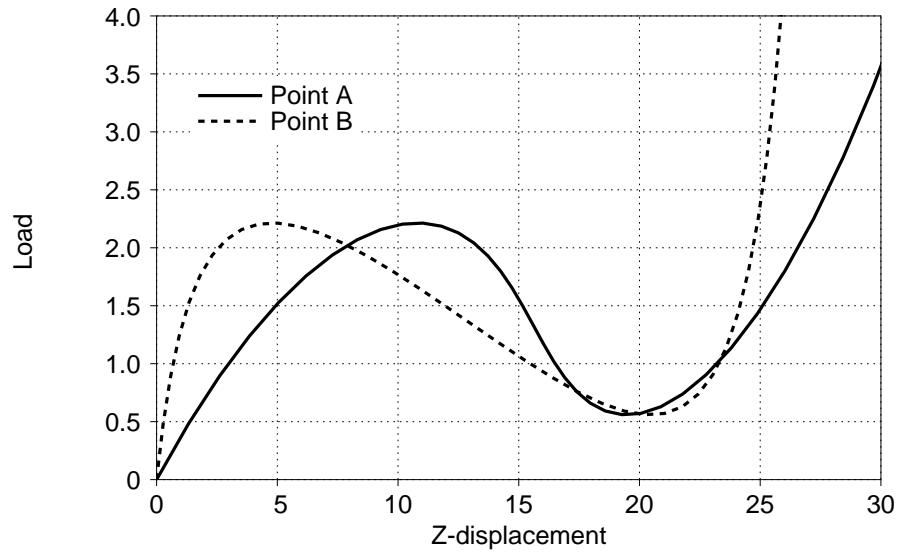


Figure 8.4. Vertical deflection at points A and B for hinged cylindrical panel with $t = 12.7mm$.

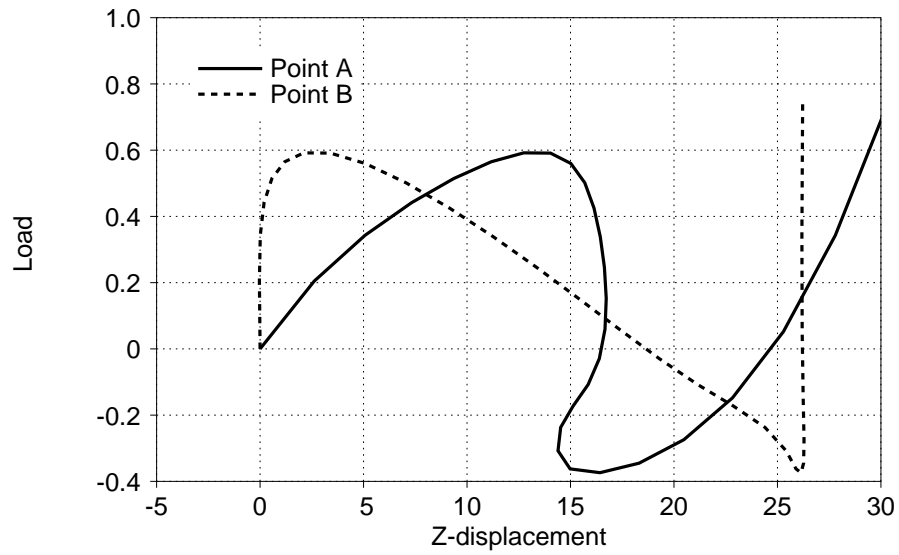


Figure 8.5. Vertical deflection at points A and B for hinged cylindrical panel with $t = 6.35mm$.

8.1.3 Pinching of a clamped cylinder.

A cantilevered cylinder is subjected to two diametrically opposite forces of magnitude F at the open end. Due to symmetry only a quarter of the structure is modelled. The problem has been studied by Stander et al. [60] and Parisch [48] using uniform element meshes. Mathisen, Kvamsdal and Okstad [43] have studied this problem using adaptive mesh techniques. The present analysis was performed using displacement control of the loaded point with 16 equal step up to a total displacement of 1.6 times the radius of the cylinder.

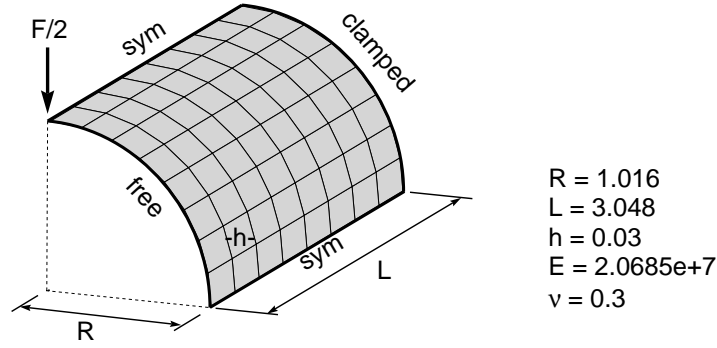


Figure 8.6. Geometry and material properties for the pinched cylinder problem.

This example shows that the ANDES4 element is better than the ANDES3 element with respect to membrane strain gradients. A mesh of 16×16 ANDES3 elements diverges before the analysis is completed, whereas a mesh of 16×16 ANDES4 elements is sufficient to complete the analysis as shown in Figure 8.7. The results in Figure 8.7 shows good agreement with the results obtained by Stander et al. [60] and Parish [48], both of whom used quadrilateral elements.

8.1.4 Stretched cylinder with free ends.

An open cylinder with free ends are subjected to two diametrically opposite forces at the halflength. Geometric data for the cylinder are given in Figure 8.9. This problem was first discussed by Gruttman et al. [32], and later by Perić and Owen [50]. Figure 8.10 shows the results of the present analysis with a mesh of 8×16 ANDES4 elements compared with Perić and Owens analysis using a mesh of 10×20 elements. The displacement of the loaded point agrees well with the results reported in [50] .

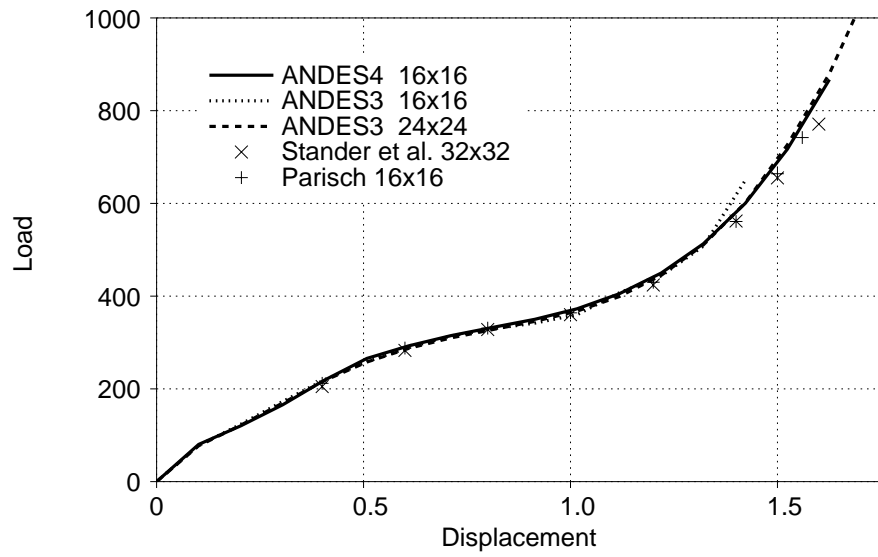


Figure 8.7. Vertical displacement at loading point for the pinched cylinder problem.

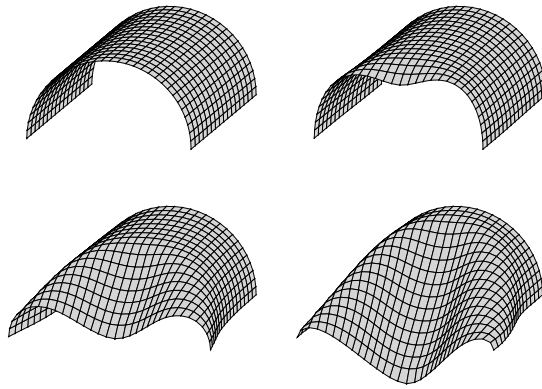


Figure 8.8. Deformed finite element mesh at various loads.

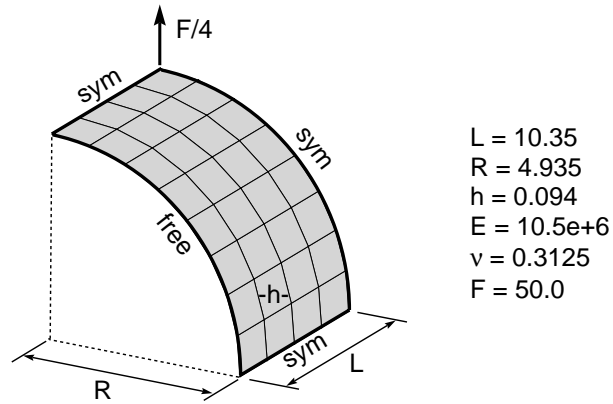


Figure 8.9. Geometry and material properties for the stretch cylinder problem.

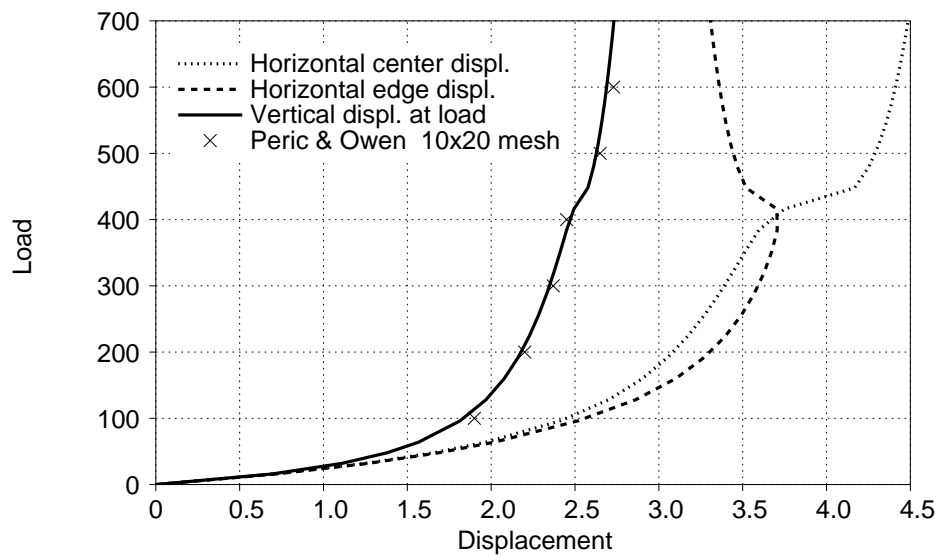


Figure 8.10. Load displacement curves for the stretched cylinder problem.

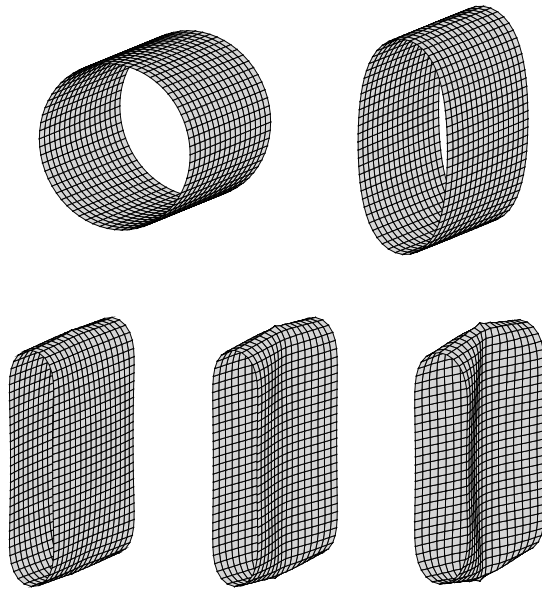


Figure 8.11. Deformed finite element mesh at various loads.

8.2 Path-following problems with bifurcation.

8.2.1 Post-buckling analysis of square plate compressed in one direction.

The geometry and material properties of the square plate are presented in Figure 7.1. The applied load is normalized with respect to the analytical buckling load for this problem given in equation (7.1.1) .

The post-buckling analysis is performed in order to evaluate the stiffness properties of the plate after bifurcation is encountered. One has used a 8×8 mesh of ANDES4 elements over the quarter model. This mesh gave about 1% error in determining the linearized buckling load.

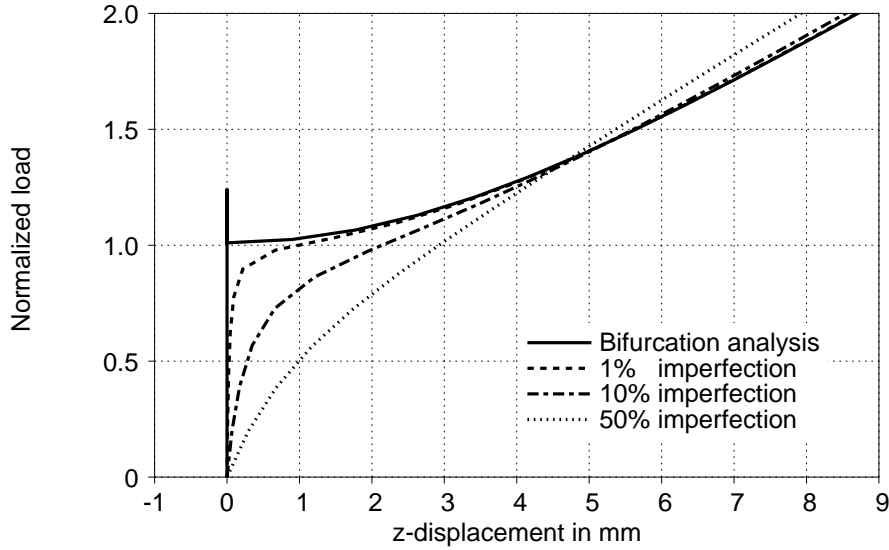


Figure 8.12. Out of plane displacement at plate center for square plate subjected to compression.

As seen in the load displacements curves in Figure 8.12 the structure shows a stable post-buckling response where it can withstand increased load after bifurcation. Figure 8.12 also shows the response of the plate with various geometric imperfection levels. The buckling mode of the structure has been scaled so that the largest out of plane imperfection is equal to 1%, 10% and 50% of the plate thickness.

8.2.2 Post-buckling analysis of shear loaded square plate.

The geometry and material properties of the square plate are described in Figure 7.3. The applied load is normalized with respect to the analytical buckling load $N_{xy_{cr}} = 105.5 \frac{N}{mm}$.

A 16×16 mesh of ANDES3 elements over the quarter model is used. This mesh gave about 5% error in determining the linearized buckling load. It should be noted that the shear loaded plate has traditionally been a difficult problem for triangular elements.

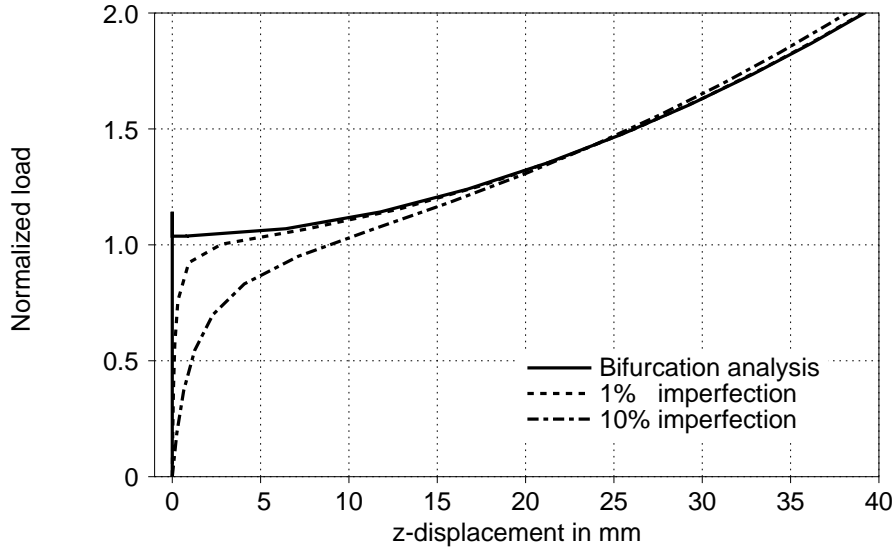


Figure 8.13. Out of plane displacement at plate center for square plate subjected to compression.

As seen in the load displacements curves in Figure 8.13 the structure shows a stable post-buckling response where it can withstand increased load after bifurcation. Figure 8.13 also shows the response of the plate with various geometric imperfection levels. The buckling mode of the structure has been scaled so that the largest out of plane imperfection is equal to 1% and 10% of the plate thickness.

8.2.3 Buckling of a deep circular arch.

This problem of snap-through of a deep circular arch has been investigated by Huddleston [37]. The asymmetric displacement path has been studied by Simons et al. [59] and Feenstra and Schellekens [23] using a small geometric imperfection to induce the buckling mode. Bjærnum [17] analyzed the problem using branch switching to follow the secondary path. The present analysis follows Bjærnum's in that no imperfection is used, and the branch switching algorithm has been used to traverse the bifurcation and continuing along the secondary path.

The dimensions of the arch are given in Figure 8.14. The arch has hinged boundary conditions at both ends and is modelled using 20 quadrilateral shell elements with the z displacements constrained.

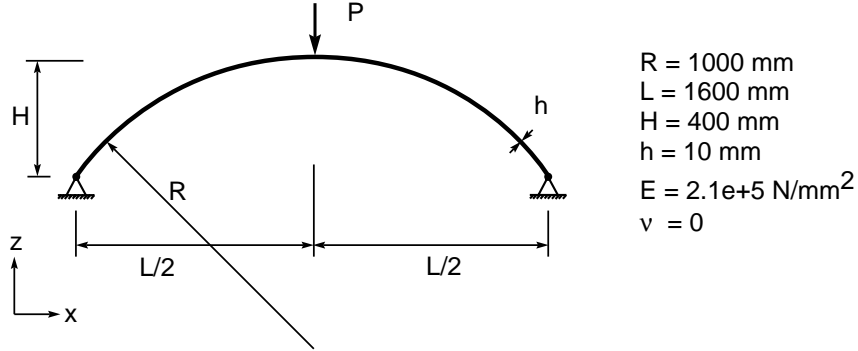


Figure 8.14. Geometry and material properties for the deep circular arch.

Figure 8.15 shows the response of the structure for the primary path, and the secondary path obtained by doing a branch switching at the first bifurcation point at $\frac{PR^2}{EI} = 13.2$. Bjærnum reports a bifurcation point at $\frac{PR^2}{EI} = 12.0$, and from his plot of the secondary path one can see that the load then jumps to approximately 13.0. Such a gap between detected and converged bifurcation points as reported by Bjærnum can indicate an inconsistent tangent stiffness matrix. The deflections of these paths are also illustrated in Figure 8.16

The problem displays some puzzling behaviour. For instance, the primary path appears not to intersect with the secondary path. The primary path keeps doing spiraling motions for the vertical displacement versus load as plotted in Figure 8.17. For each spiraling motion another wavelike deformation is

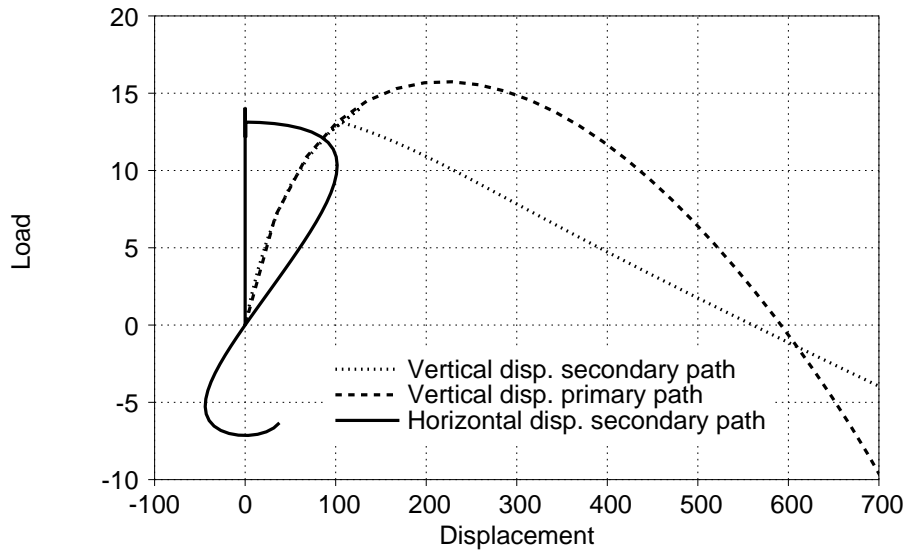


Figure 8.15. Displacements for the primary and secondary paths.

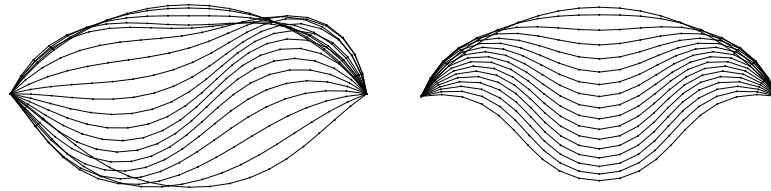


Figure 8.16. Deformations for the secondary and primary paths.

fed into the arch as shown in Figure 8.18. The fact that the primary and secondary path do not intersect can be discerned from the fact that the primary path never achieves the same vertical deflection for the midpoint of the arch as the secondary path.

The secondary path keeps doing figure-of-eight like motions for the midpoint of the arch. The branch switching algorithm does not pick up a new bifurcation point at the bottom point of the secondary path as would be expected.

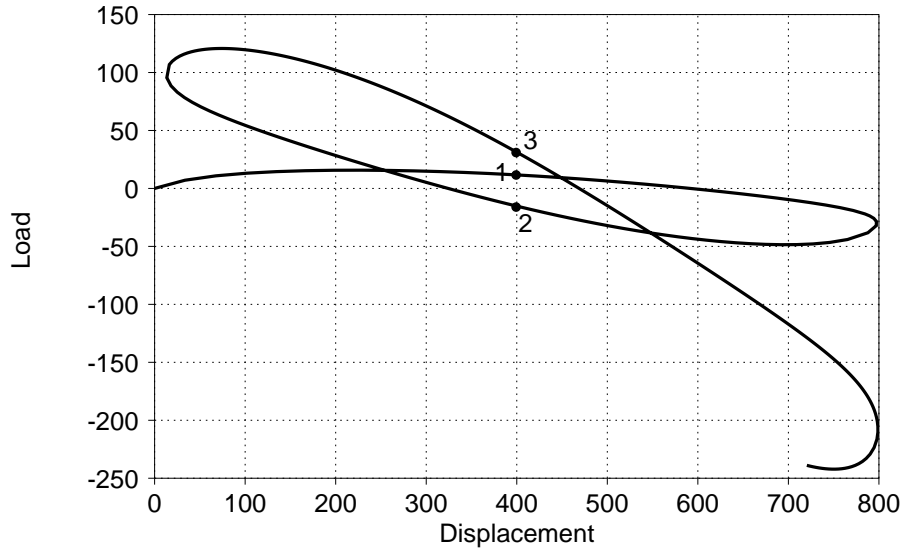


Figure 8.17. Vertical displacement for the primary path. Numbers 1 2 and 3 show the location of the deformed element geometries in Figure 8.18.

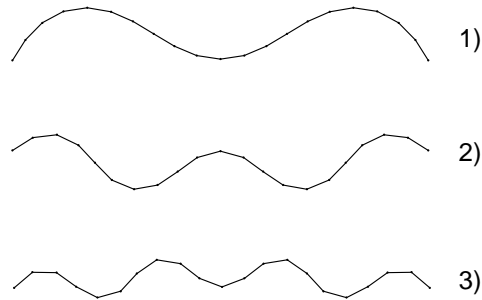


Figure 8.18. Displacements for the primary path. Numbers refer to the load-displacement curves in Figure 8.17.

This conclusion seems to agree with Bjærum, since no such bifurcation point is reported. The “mismatch” is a surprise since one expects the structure to be able to pick up additional load once it hits bottom. But detecting and switching to the new stable path seems to be computationally difficult.

8.2.4 Right angle frame subjected to in-plane load.

The right angle frame in Figure 8.19 is subjected to a in-plane load. The applied load acts on the lower corner of the tip. This problem has been studied by Nour-Omid and Rankin [46] in the post-critical domain.

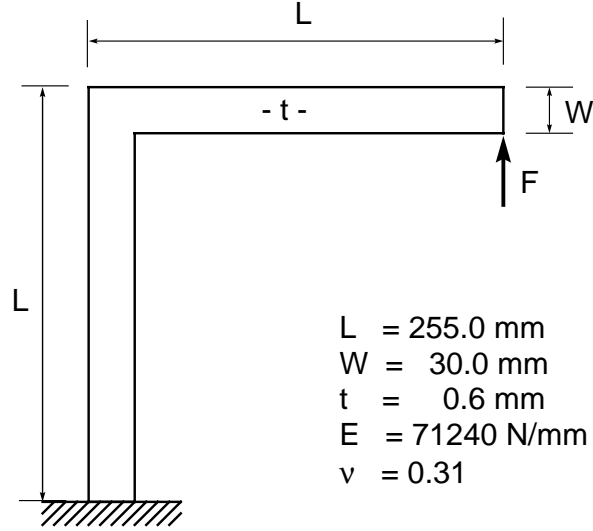


Figure 8.19. Geometry and material properties for the right angle frame.

Table 8.2 lists the critical loads given by different element types and mesh refinements. Results from Nour-Omid and Rankin are included in Table 8.2 for comparison. The postcritical response for the structure is shown in Figure 8.20 for different element meshes with ANDES3 and ANDES4 elements.

Table 8.3 gives the number of steps and iterations for this problem with the various consistent formulations. The convergence rates are measured at the stable “upswing” section of the equilibrium path. For large sections of the analysis this convergence rate is not obtained due to ill-conditioning at the “flat” section of the equilibrium path.

Table 8.2. Critical load for the right angle frame.

Element type	Num. of elements	F_{cr}
ANDES3	17×2	1.164
ANDES3	68×2	1.142
ANDES3	153×2	1.135
ANDES4	17	1.146
ANDES4	68	1.134
ANDES4	153	1.130
Nour-Omid & Rankin [46]	17	1.138
Nour-Omid & Rankin [46]	64	1.130

Table 8.3. Convergence of the 17×2 ANDES3 mesh.

Formulation	Symmetric stiff.			Non-symmetric stiff.		
	N.steps	N.iter.	C.rate.	N.steps	N.iter.	C.rate.
C	18	179	L.	18	152	Q.
CSE	18	174	Sl.	18	145	Q.
CSSE	18	145	Q.	18	145	Q.

Figure 8.20. Post buckling response for the right angle frame.

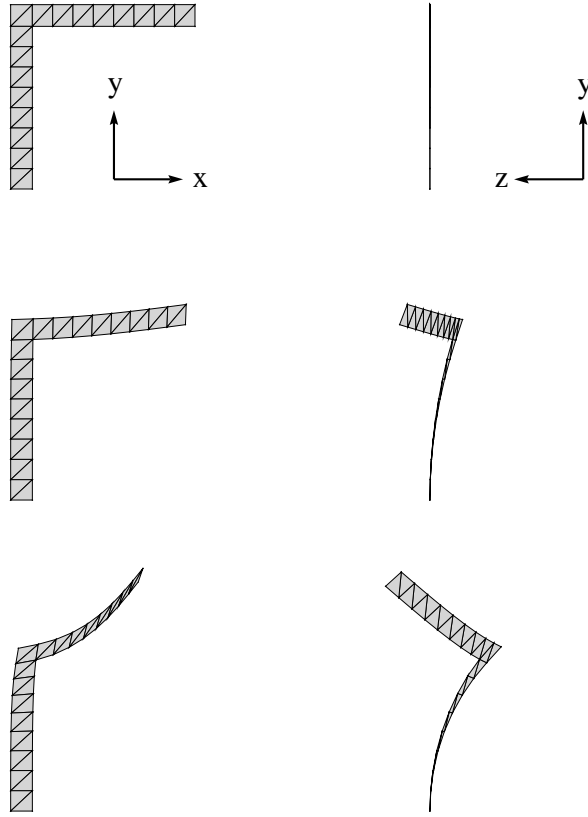


Figure 8.21. Deformations for $F = 1.164$, $F = 1.26$ and $F = 2.0$ with a mesh of 17×2 ANDES3 elements.

8.2.5 Right angle frame subjected to end moments.

The following two problems were modeled with the beam elements described in Appendix 1. The problems were included in the present work because of the numerical challenges they offer as regards branch switching and continuation algorithms.

The right-angle frame subjected to end moments was first introduced by Argyris [3] and later studied by Nour-Omid and Rankin [46]. The frame has been modeled using 10 Timoshenko beam elements for a half model. Beam elements have been chosen to model the frame since the moment loads are impossible to introduce for shell elements without using follower forces that are non-conservative and hence introduce follower-load stiffness matrix. Such a contribution has not been implemented for the shell elements developed in this work.

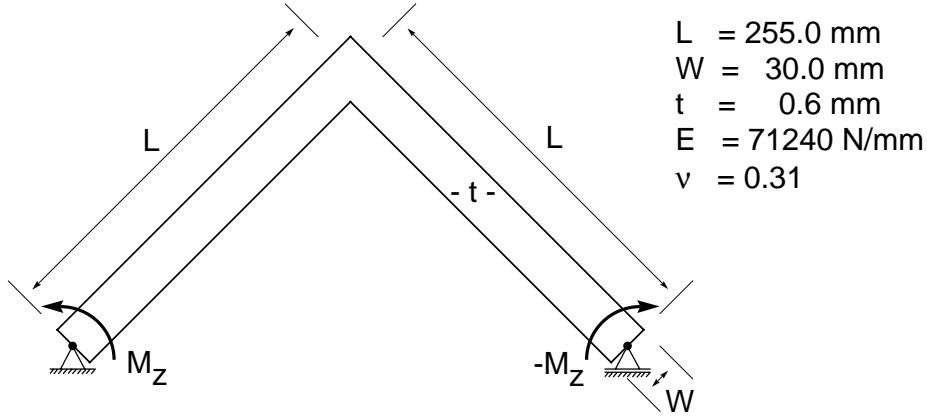


Figure 8.22. Geometry and material properties for the symmetric frame.

The response of the structure displays two distinct equilibrium paths. The primary path has only displacements in the x - y plane, whereas the secondary path switches to out of plane displacements after bifurcation. The response shows that the frame rotates a full 360° as the frame ends rotate through a full circle about the z axis. Finally the frame rotates back to the x - y plane with the load reversed. The out of plane bifurcation happens at $M_z = \pm M_{cr} = 6.464 \text{ Nmm}$. The analysis can be run repeated indefinitely. If the bifurcation starts at $M_z = +M_{cr}$ a full out of plane revolution will be obtained at $M_z = -M_{cr}$. A second revolution will then take place after which the structure finally returns to the same configuration of the first bifurcation with load $M_z = +M_{cr}$.

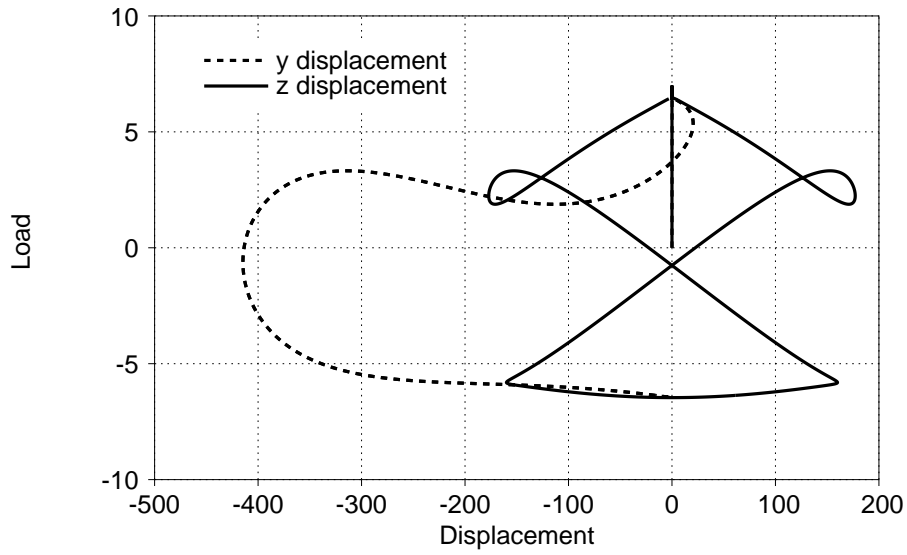


Figure 8.23. y and z displacements for the apex of the right angle frame.

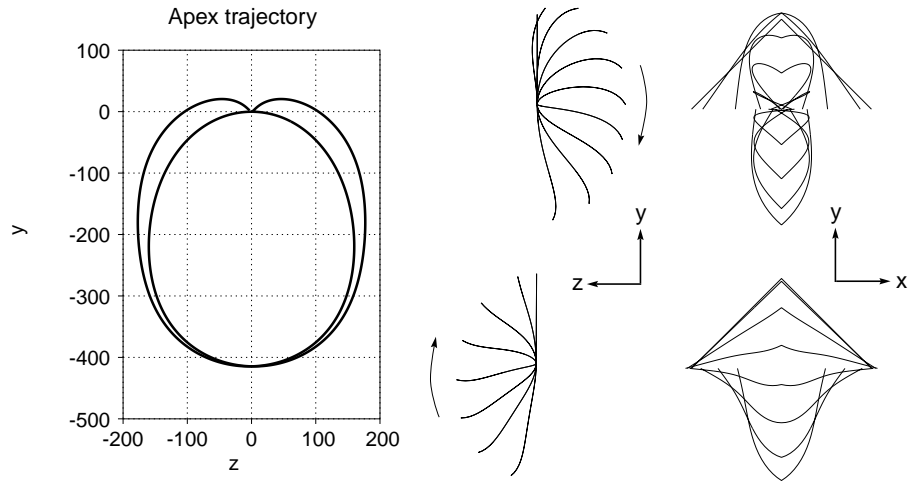


Figure 8.24. Deformations for the for the frame subjected to end moments. Arrows indicate direction of motion.

8.2.6 Cable Hockling.

An initially straight cable is subjected to a tip torsional moment. One end of the cable is fully clamped, whereas the loaded tip is free to rotate about the

longitudinal x axis, and moves along it. No rotation is allowed about the y and z axes at the loaded end. The material and geometrical properties of the cable are defined in Figure 8.25. The Euler-Bernoulli beam element described in Appendix 1 is used to discretize the cable.

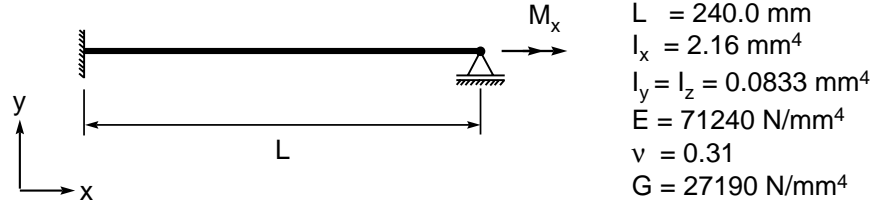


Figure 8.25. Cable geometry and material properties.

This problem was first studied in the postbuckling regime by Nour-Omid and Rankin [46]. The cable exhibits linear response with twisting and no lateral displacement up to the bifurcation point. After bifurcation the cable forms a loop with the loaded end moving towards the clamped end. Finally a full circular loop is formed after the path has traversed a second bifurcation point and the applied load returns back to zero.

The analysis is made more stable by restricting the midpoint of the cable from moving out of the x - y plane. The position of the loop is otherwise undetermined in the y - z plane. The equilibrium path has been followed without this restriction, but the convergence rate is impaired. This additional boundary condition is consistent with that used by Nour-Omid and Rankin.

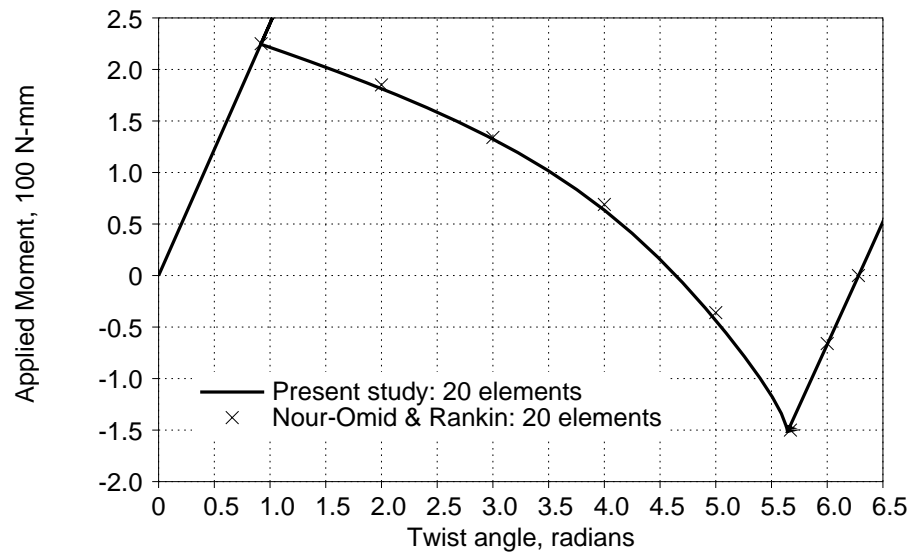


Figure 8.26. Cable hockling. Moment versus tip rotation.

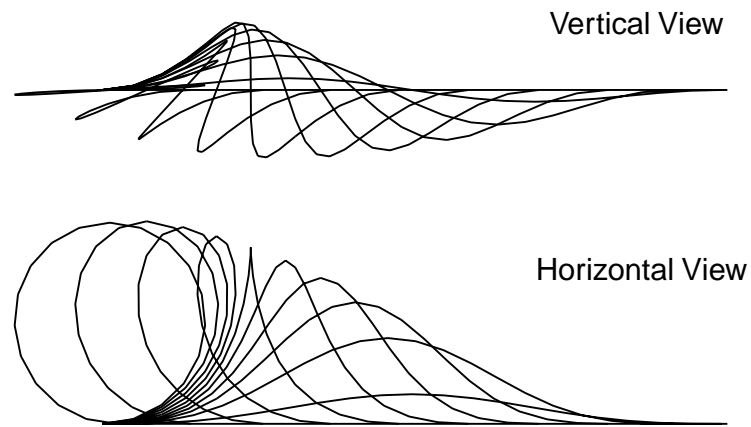


Figure 8.27. Deformations for the for the cable subjected to end moment.